iScience

Article

One-step depositing method of PAni/MnO_2 composites for enhanced supercapacitor performance

Graphical abstract

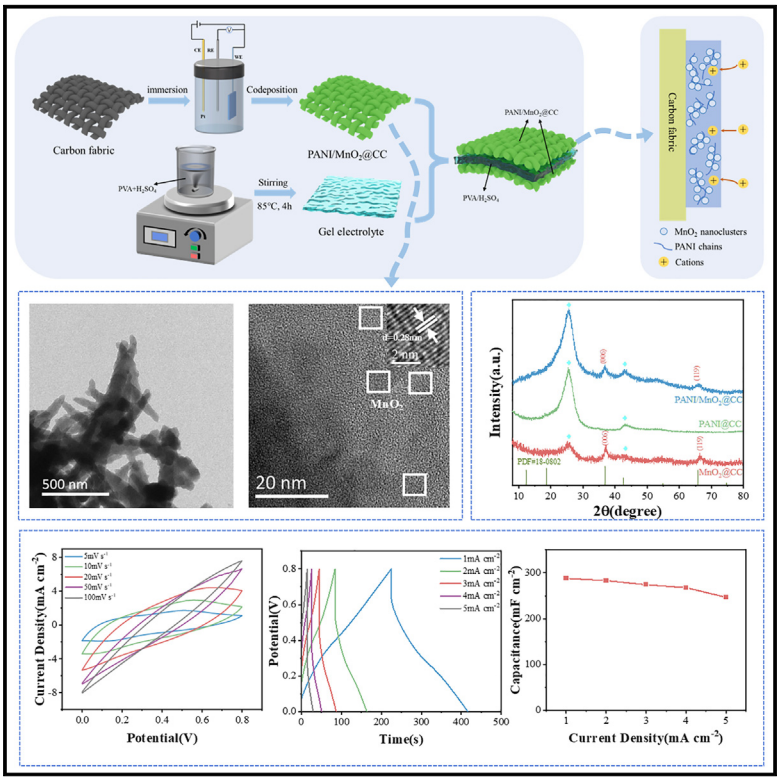

Highlights

- A simple and promising method to fabricate a PAni/MnO_2 composite was proposed
- PAni skeleton can enhance the conductivity and electroactive surface area of the composite
- The effect of process parameters on the electrochemical performance was explored
- The PAni/MnO_2@CC as SC electrodes exhibits an excellent electrochemical performance

Authors

Shuang Xi, Xiaoli Qian, Ximing Cheng, Huilong Liu, Homa Shabanzadeh, Davoud Dastan

Correspondence

shuangxi@njfu.edu.cn (S.X.), huilong.liu@gdut.edu.cn (H.L.)

In brief

Energy application; Energy storage; Energy systems

Xi et al., 2025, iScience *28*, 111774
February 21, 2025
https://doi.org/10.1016/j.isci.2025.111774

CellPress

iScience

CellPress
OPEN ACCESS

Article

One-step depositing method of PAni/MnO_2 composites for enhanced supercapacitor performance

Shuang Xi,[1,5,*] Xiaoli Qian,[1] Ximing Cheng,[1] Huilong Liu,[2,*] Homa Shabanzadeh,[3] and Davoud Dastan[4]
[1]College of Mechanical and Electronic Engineering, Nanjing Forestry University, Nanjing, China
[2]State Key Laboratory of Precision Electronic Manufacturing Technology and Equipment & School of Electromechanical Engineering, Guangdong University of Technology, Guangzhou, China
[3]Department of Physics, University of Zanjan, Zanjan, Iran
[4]Department of Materials Science and Engineering, Cornell University, Ithaca, NY, USA
[5]Lead contact
*Correspondence: shuangxi@njfu.edu.cn (S.X.), huilong.liu@gdut.edu.cn (H.L.)
https://doi.org/10.1016/j.isci.2025.111774

SUMMARY

Manganese dioxide (MnO_2) is extensively used in supercapacitors, but its poor conductivity and low power density limit its applications. This study employed a one-step electrochemical deposition method to fabricate a polyaniline (PAni)/MnO_2/carbon cloth (CC) composite electrode, which was assembled into flexible supercapacitors. Optimal process parameters were determined through exploring the effect of deposition durations on the electrochemical performance. With optimized synergistic effects between the components, the PAni/MnO_2@CC composite electrode exhibits high specific capacitance of 1,694.25 mF cm^{-2} at 1 mA cm^{-2}, which is remarkably better than that of PAni@CC, MnO_2@CC, and other reported PAni-based electrodes. The assembled supercapacitor displays high energy density, superior bending performance, and good cycle stability. This easy-to-prepare composite electrode, with excellent energy storage capability, offers significant potential for flexible energy storage devices.

INTRODUCTION

The rapid development of wearable electronic devices has significantly increased the demand of flexible energy storage devices, such as batteries and supercapacitors, among which supercapacitors have been proved to be excellent power sources due to their environmental friendliness, rapid charge/discharge capabilities, high power density, and extremely long cycle life.[1] Based on their energy storage mechanisms, supercapacitors can be categorized into electrical double-layer capacitors (EDLCs)[2,3] and pseudocapacitors.[4] EDLCs store energy through a physical process that involves the adsorption of ions from the electrolyte onto the surface of the electrodes. In contrast, pseudocapacitors primarily involve electron transfer and redox reactions occurring within the electrode materials,[5] which enables them to achieve superior capacitive performance.

The two main types of electrode materials employed in pseudocapacitors are transition metal compounds (such as metal oxides,[6,7] carbide,[8] phosphide,[9] nitride,[10] and boride[11,12]) and conductive polymers (such as polyaniline [PAni], polypyrrole, and polythiophene).[13–15] Nowadays, transition metal phosphides/borides serving as the pseudocapacitive materials have attracted considerable scientific attention owing to their superior electrical conductivity, high theoretical capacity, and prominent thermal stability. Whereas, the low-cost engineering of transition metal phosphides/borides with specific composition and structure as well as satisfying electrochemical performance remains a knotty problem. Among these transition metal compounds, manganese dioxide (MnO_2)[16,17] offers a high theoretical specific capacitance, abundant surface area, and low production cost. However, its low conductivity severely limits its widespread applications. On the other aspect, PAni[18,19] demonstrates excellent reversible electrochemical properties and good ionic conductivity, facilitating charge transfer and storage, thereby enhancing the energy density and charge-discharge efficiency of supercapacitors. Nevertheless, PAni suffers from volume changes during the charge/discharge process and the burial of active sites due to agglomeration, resulting in poor rate performance and low specific capacitance. In order to achieve the complementary advantages of the two materials, a plenty of research studies are focused on composite materials consisting of MnO_2 and PAni applied to supercapacitors. Sun et al.[20] synthesized MnO_2/PAni electrode materials by redox and chemical oxidative polymerization methods, with a specific capacitance of 565 F g^{-1} at a current density of 0.8 A g^{-1} and a capacitance retention of 77% after 1,000 cycles at 8 A g^{-1}. Zhu et al.[21] synthesized the PAni@γ-MnO_2/carbon cloth (CC) electrode by hydrothermal and electropolymerization methods with a specific capacitance of 1,105 mF cm^{-2} at a current density of 1 mA cm^{-2} in 1 M H_2SO_4. It has been proved that the MnO_2/PAni

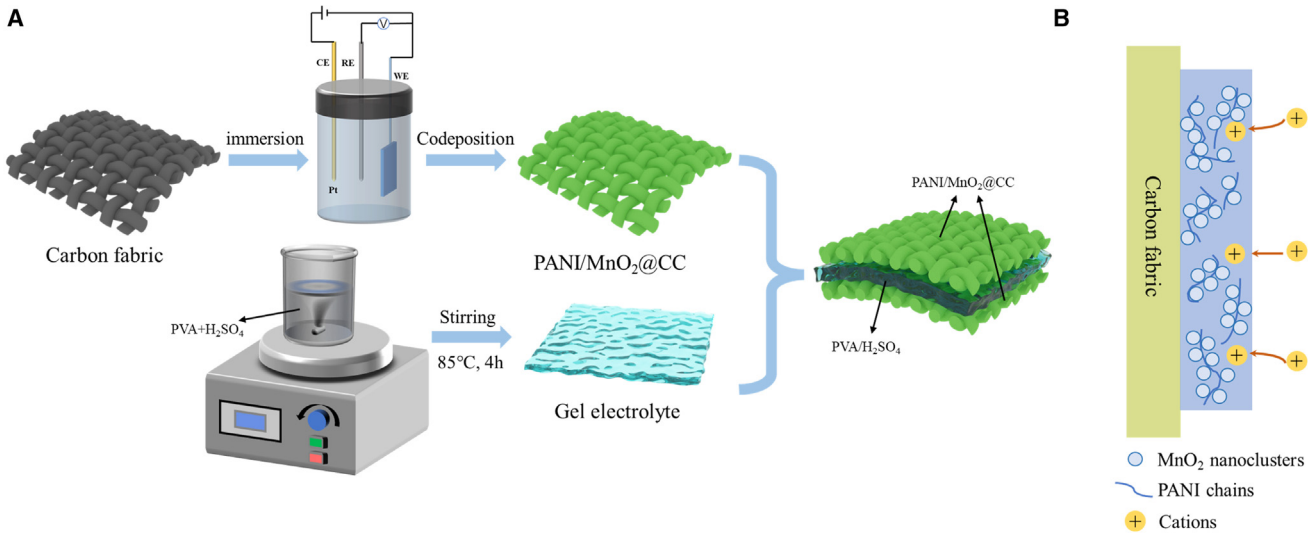

Figure 1. Schematic of electrode preparation and device charge storage mechanism

(A) Schematic diagram of the preparation process of PAni/MnO_2@CC electrodes and symmetric supercapacitors.

(B) Ion transferring mechanism in the composite electrode.

hybrid electrode can make full use of both components, and thus improve the electrochemical performance of the assembled supercapacitors. Despite these advances, existing methods often involve complex, multi-step processes that require oxidizing agents, limiting their scalability and cost-effectiveness. Therefore, it is of great practical significance to study and develop PAni/MnO_2 composite materials with simple synthesis methods along with excellent electrochemical properties.

In this work, a simple and efficient one-step deposition method was employed to directly synthesize PAni/MnO_2 composites onto CC substrates without the usage of binders, which would simplify the fabrication process and at the same time ensure excellent conductivity together with adequate active surface areas. Furthermore, MnO_2 nanoparticles within the PAni membrane can effectively alleviate the volume change, thereby to obtain synergistic electrochemical performance superior to the sole component. By systematically analyzing the structure-performance relationship, the material preparation process was optimized, and then high-performance electrodes were developed and assembled into supercapacitors. The resulting devices exhibit superior specific capacitance, excellent stability, and significant potential for scalable production, addressing critical challenges in energy storage applications. This innovative approach not only advances the state of the art in PAni/MnO_2[22] composites but also provides a practical pathway for developing next-generation energy storage technologies. Schematic of electrode preparation and device charge storage mechanism is shown in Figure 1.

RESULTS

Material characterization of PAni/MnO_2 deposited on CC

The morphology of MnO_2@CC, PAni@CC, and PAni/MnO_2@CC is shown in Figure 2. As shown in Figure 2A, uniform and dense MnO_2 nanoparticles have been grown on CC.[23] The enlarged SEM image in Figure 2D reveals that the MnO_2 film consists of numerous nanorods, which exhibit a rough, uniform, and worm-like shape. Additionally, some sea urchin-like clusters are observed on the MnO_2 film, which likely result from the self-agglomeration of nanorods in the deposition solution. Figures 2B and 2E present the densely distributed morphology of PAni on CC, where more ordered and regular nanorods with diameters of approximately 50 nm are visible. Figures 2C and 2F demonstrate that after co-deposition of PAni/MnO_2, the composite exhibits a typical irregular morphology, with a significantly increased fibrous structure thickness. Unlike the MnO_2@CC and PAni@CC samples, the PAni/MnO_2 composite tends to form an interconnected membrane, which not only creates a more abundant electroactive surface and improves electrical conductivity through continuous film formation but also buffers the volume changes resulting from repeated ion insertion and extraction.

To further characterize the PAni/MnO_2@CC composites, transmission electron microscopy (TEM) measurements were conducted. As shown in Figure 3A, MnO_2 exhibits a spheroidal flower-like shape, with irregular stacking of ultra-thin nanosheets on the outer ring of the spheroid, which makes the distribution of small crystalline domains more pronounced. Figure 3B shows that PAni exhibits a distinct nanorod structure, consistent with the SEM results of PAni. In the TEM images of the PAni/MnO_2 composites in Figures 3C and 3D, it can be observed that MnO_2 particles are distributed on the surface of the rod-shaped PAni, with some MnO_2 also being wrapped by PAni. This not only increases the specific surface area of the PAni/MnO_2 composite but also provides abundant electrochemically active sites, further enhancing the electrochemical properties of the material. The high-resolution TEM (HRTEM) image (Figure 3D) reveals that MnO_2 nanoparticles with a typical size of ~10 nm are encapsulated by amorphous PAni, resulting in the unapparent layered structure of the MnO_2 due to the shielding of PAni. The inset of

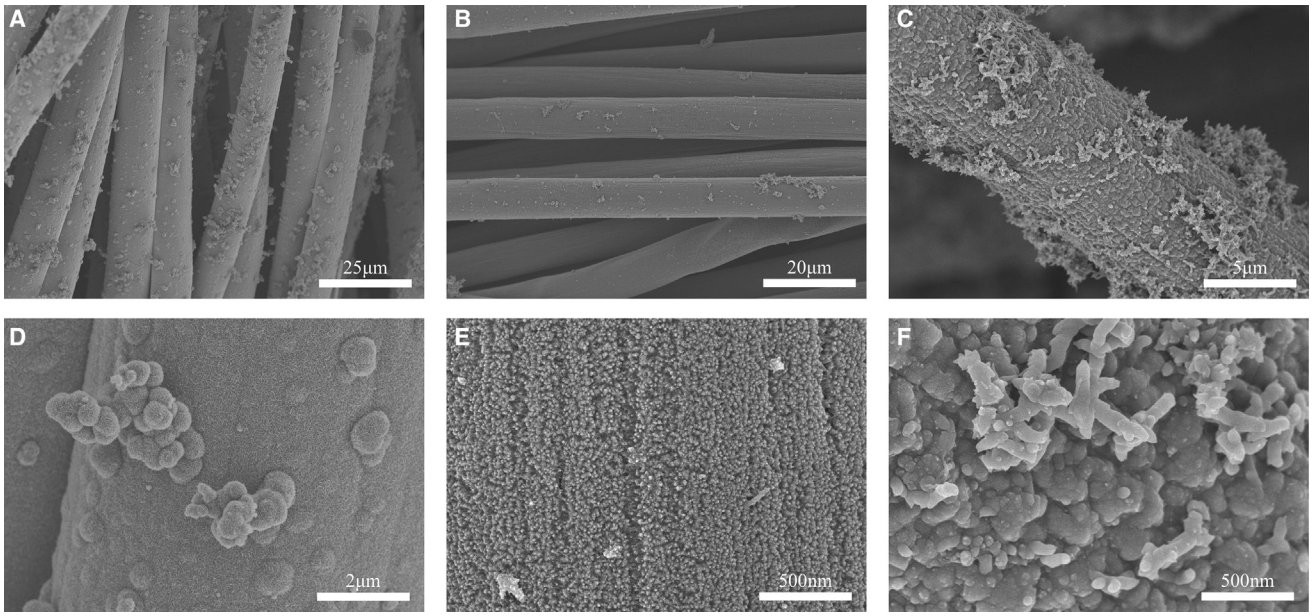

Figure 2. SEM images of three different electrodes

(A and D) SEM images of MnO_2@CC.

(B and E) SEM images of PAni@CC.

(C and F) SEM images of PAni/MnO_2@CC.

Figure 3D shows the enlarged view of MnO_2 nanolayers, showing their interlayer space of ~0.28 nm. The observation reveals that MnO_2 particles are uniformly distributed and exhibit typical nanoscale features, indicating good synthetic control. Furthermore, the interface between the MnO_2 layer and the PAni matrix is clearly visible, suggesting strong interactions and interface bonding between PAni and MnO_2.

The composition of the obtained electrodes was characterized using X-ray diffraction (XRD), as shown in Figure 4A. All three patterns exhibit the representative graphitic carbon diffraction peaks at 25.52° and 43°, which can be attributed to (002) and (100/101) crystal planes, respectively. The MnO_2@CC material shows typical peaks at 36.84° and 66.43°, corresponding to the (006) and (119) crystal planes of MnO_2 (JCPDS card number PDF # 18-0802), respectively. The weak peak may be attributed to the poor crystallinity and fine grain size of MnO_2. For PAni@CC, a broad peak appears in the range of 20°–25°, which is characteristic of the amorphous nature of PAni. The PAni/MnO_2@CC composite possesses all the characteristic peaks of MnO_2@CC and PAni@CC with no displacement occurred, verifying the successful deposition of PAni and MnO_2 via the co-deposition method.

Figure 4B presents the X-ray photoelectron spectroscopy (XPS) survey spectrum of PAni/MnO_2@CC, in which four elements of Mn, O, N, and C could be observed. The Mn element originates from MnO_2, while the C element comes from CC. The high-resolution C 1s spectrum in Figure 4C displays two peaks at 284.8 and 285.9 eV,[24] corresponding to non-oxygenated carbon (C–C/C=C) and oxygenated carbon (C–O), respectively. In the high-resolution O 1s spectrum shown in Figure 4D, three distinct peaks are observed, corresponding to Mn–O–Mn (529.2 eV), Mn–O–H (530.5 eV), and H–O–H (532.2 eV).[25] Figure 4E shows the deconvoluted N 1s spectrum, revealing four peaks located at 396.9, 398.1, 399.4, and 402.5 eV. These peaks correspond to =N–, –NH–, $–NH^+–$, and $=NH^+–$, respectively, with the presence of $–NH^+–$ and $=NH^+–$ indicating that PAni is in a doped state. Figure 4F displays the high-resolution Mn 2p spectrum, with two peaks at 641.7 and 653.4 eV, corresponding to Mn 2p3/2 and Mn 2p1/2, respectively. The orbital splitting energy between Mn 2p3/2 and Mn 2p1/2 is 11.7 eV,[26,27] confirming the presence of Mn^{4+} ions and indicating the presence of MnO_2 in the material.

Electrochemical performances of electrodes

To investigate the effect of deposition time on the properties of PAni/MnO_2@CC electrodes, three samples, i.e., PAni/MnO_2@CC-100 s, PAni/MnO_2@CC-300 s, and PAni/MnO_2@CC-500 s, were tested using three-electrode system in 1 M H_2SO_4 electrolyte. Figure 5A presents the cyclic voltammetry (CV) curves of the obtained samples at a scan rate of 5 mV s^{-1} within a potential range of −0.2 to 0.8 V. The results show that the background current significantly increases when the deposition time is extended from 100 to 300 s. However, when the deposition time is further increased to 500 s, the background current noticeably decreases, indicating that 300 s is the optimal deposition duration. The comparative galvanostatic charge-discharge (GCD) curves of the ternary composites tested at a current density of 1 mA cm^{-2} are shown in Figure 5B. All discharge curves exhibit an approximately linear shape with a slight bending at the beginning, which can be attributed to the pseudocapacitive property of PAni. Among the samples, PAni/MnO_2@CC-300 s shows the longest discharge time, indicating the highest specific

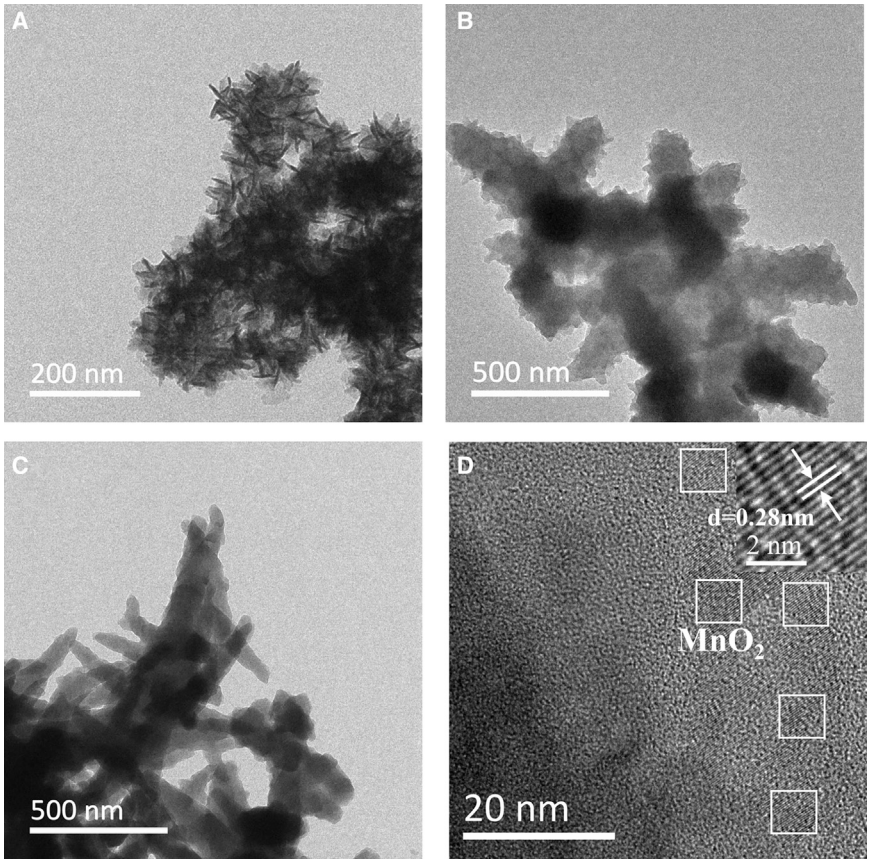

Figure 3. TEM images of three different electrodes

(A) TEM image of MnO_2@CC.

(B) TEM image of PAni@CC.

(C) TEM image of PAni/MnO_2@CC.

(D) HRTEM image of PAni/MnO_2@CC. The white outlines are used to clarify the distribution of MnO_2 nanoparticles.

capacitance, which is consistent with the CV results. The specific capacitance decreases from 300 to 500 s, possibly due to the more compacted active material deposited on CC leading to reduced active sites and lower electrochemical utilization efficiency.[28]

Since PAni/MnO_2@CC-300 s exhibits the best electrochemical performance, it was selected for the subsequent tests. Figure 5C shows the CV curves of PAni/MnO_2@CC-300 s at different scan rates ranging from 5 to 100 mV s^{-1}. As the scan rate increases, an increase in peak current is observed, indicating good ion diffusion dynamics and ideal capacitive performance. With higher scan rates, the oxidation peak shifts positively, and the reduction peak shifts negatively, due to the increased ion transport resistance within the electrode. However, at the high scan rate of 100 mV s^{-1}, the redox peaks disappear, and the voltammogram distorts from the typical rectangular shape, likely due to the limitations of the electrochemical reaction rate and ion diffusion. Although the electrode exhibits some shape distortions in the voltammograms, these occur only at scan rates higher than 50 mV s^{-1}, suggesting that the composites maintain good electroactivity. The GCD curves at various current densities in Figure 5D show that GCD profiles at high current density take the form of symmetrical triangles, confirming ideal electrochemical reversibility and fast reaction kinetics.

To verify the synergistic effect of PAni and MnO_2 on the electrode performance, comparative electrochemical tests were conducted on MnO_2@CC, PAni@CC, and PAni/MnO_2@CC-300 s. The CV results in Figure 6A show that all CV curves of PAni-based electrodes exhibit two distinct pairs of redox peaks, which are related to the redox transition of PAni between the leucoemeraldine form and the protonated emeraldine form, the transformation of the *p*-benzoquinone/hydroquinone couple,[29,30] and the redox transition between emeraldine and pernigraniline. The merging of these redox peaks with a high background current density indicates the typical pseudocapacitive performance of PAni.[31] In comparison, the CV curve of MnO_2@CC displays a much smaller area, illustrating its significantly lower capacitance. The peak current of PAni/MnO_2@CC is higher than that of the individual materials, indicating the largest specific capacitance of PAni/MnO_2@CC. The maximum capacitance value of the hybrid electrode is caused by the synergistic action of various components. CC provides high specific surface area with its 3D textile structure. PAni framework can not only increase the pseudocapacitance but also improve the conductivity of the electrode. MnO_2 takes an important part in improving specific capacitance performance. Particularly, the co-deposited PAni/MnO_2 on CC has an interconnected membrane, which could provide sufficient surface area to deliver more shuttle channels and effective ion exchange between the electrolyte and the two active materials. There is also H bonding between MnO_2 and PAni, which plays an important role in the enhanced electrochemical performance.

As seen in the GCD profiles in Figure 6B, the charge and discharge curves exhibit distinct potential platforms around 0.7 and 0.4 V, respectively, which are consistent with the anodic and cathodic peaks in the CV curves. The discharge duration of PAni/MnO_2@CC is the longest, with a calculated specific capacitance of 1,694.25 mF cm^{-2} based on Equation 1. Figure 6C shows the GCD-based areal capacitance of MnO_2@CC, PAni@CC, and PAni/MnO_2@CC at current densities ranging from 1 to 5 mA cm^{-2}, according to Equation 1. At a current density of 1 mA cm^{-2}, the areal capacitance of PAni/MnO_2@CC is calculated to be 1,694.25 mF cm^{-2}, which is significantly higher than the sum of PAni@CC (1,093.88 mF cm^{-2}) and MnO_2@CC

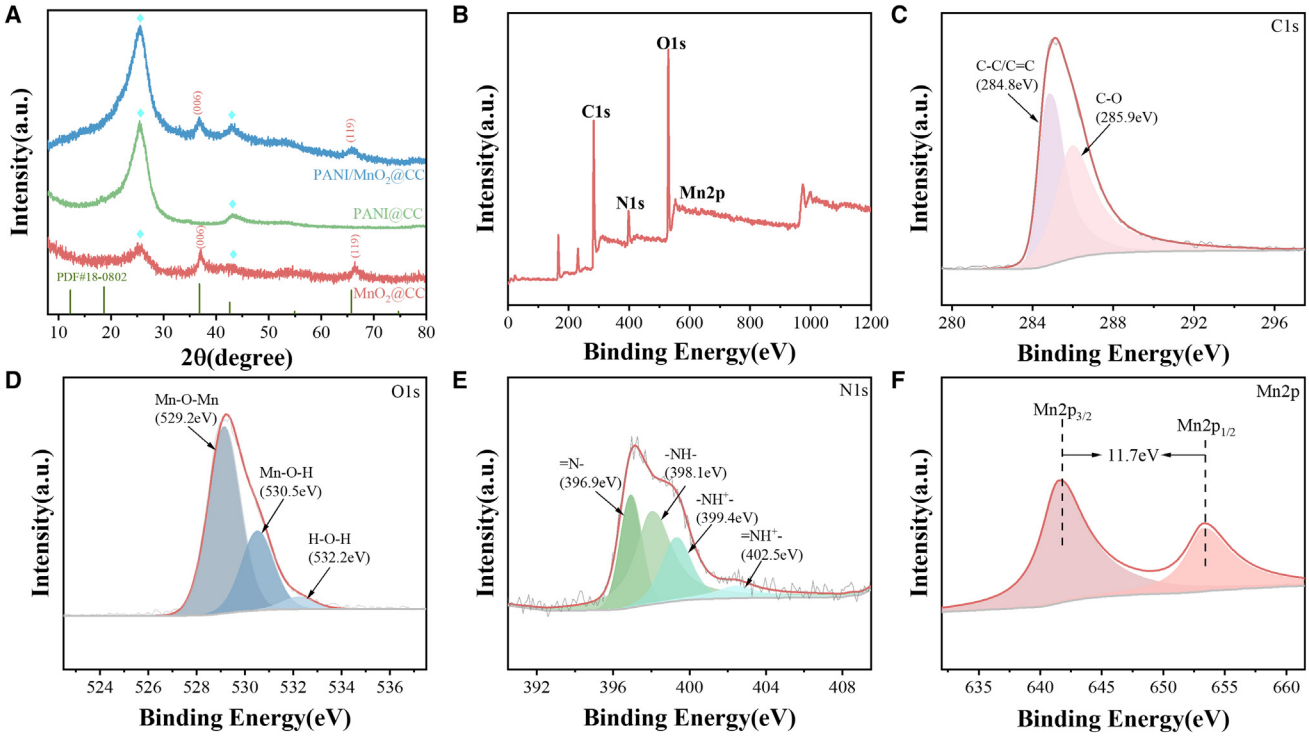

Figure 4. XRD and XPS images of the PAni/MnO_2@CC electrode

(A) XRD patterns of MnO_2@CC, PAni@CC, and PAni/MnO_2@CC.

(B) XPS survey spectrum of PAni/MnO_2.

(C) C 1s spectrum.

(D) O 1s spectrum.

(E) N 1s spectrum.

(F) Mn 2p spectrum.

(30.37 mF cm^{-2}). The capacitance retention of PAni/MnO_2@CC is 81.6% as the current density increases to 5 mA cm^{-2}, which is superior to that of the other two samples. The significantly enhanced areal capacitance and rate capability of the PAni/MnO_2@CC hybrid electrode can be attributed to the synergistic effects of the composite constituents.

Figure 6D shows the Nyquist plot obtained from electrochemical impedance spectroscopy (EIS) testing at open-circuit potential over a frequency range of 0.01–100 kHz. The curve consists of two distinct regions: the semicircle in the high-frequency region and the straight line in the low-frequency region. The intercept of the curve on the z′ axis represents the electrolyte resistance (R_s), and the charge transfer resistance (R_{ct}) can be calculated from the semicircle.[32] As shown in the inset, PAni/MnO_2@CC exhibits the lowest R_s of 1.329 Ω and R_{ct} of 0.1 Ω, indicating that the hybrid material has the best charge transfer capability, verifying the improved conductivity after PAni introduction. By linearly fitting the real part of the impedance (z′) to the −1/2 power of the angular frequency curve ($\omega^{-0.5}$) in the frequency range of 0.01–0.0825 Hz, the Warburg coefficient (σ, Ω $s^{-0.5}$) can be extracted and used to further quantitatively analyze the ionic diffusion resistance (Figure 6E).[33] The value of σ increases with the content of MnO_2, from 0.125 Ω $s^{-0.5}$ of PAni@CC to 0.812 Ω $s^{-0.5}$ of MnO_2@CC, indicating that the presence of MnO_2 results in a greater contribution from diffusion-controlled processes.

Figure 6F presents the long-term cycling performance of PAni@CC and PAni/MnO_2@CC. After 2,000 cycles, the capacitance of PAni/MnO_2@CC remains around 72.7%, while that of PAni@CC remains at approximately 54.2% in 1 M H_2SO_4 electrolyte at 5 mA cm^{-2}. PAni/MnO_2@CC exhibits enhanced cycling performance compared to PAni@CC thanks to the existence of PAni, which acts as a scaffold to improve the interfacial contact and impedance matching of MnO_2 nanoparticles, and thus to strengthen the structural stability.

To further explore the electrochemical behavior of the electrodes, a kinetic analysis was conducted.[34] In the CV tests, by analyzing the relationship between current and scan rate at different potentials, the specific capacitance in PAni/MnO_2@CC can be categorized into electric double-layer capacitance and pseudocapacitance. The relationship can be calculated using Equation 1.

$$i = av^b \quad \text{(Equation 1)}$$

where i (mA) is the peak current, v (mV s^{-1}) is the scan rate, and b are adjustable parameters. When b = 0.5, charge storage is primarily controlled by a diffusion-controlled Faradaic intercalation

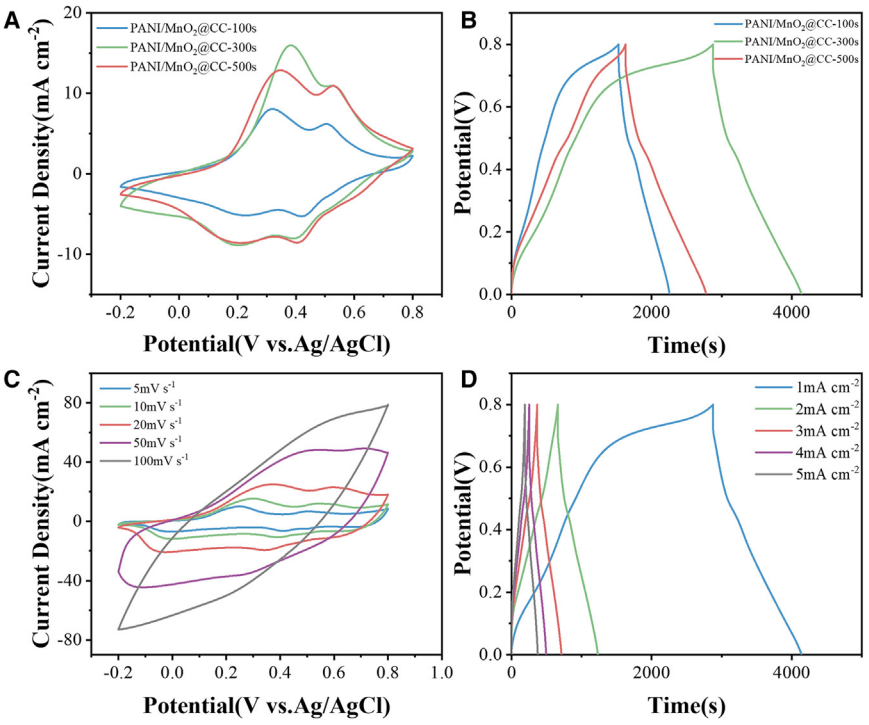

Figure 5. CV and GCD curves of electrodes with different deposition times

(A) CV curves of PAni/MnO_2@CC-100 s, PAni/MnO_2@CC-300 s, and PAni/MnO_2@CC-500 s at a scan rate of 5 mV s^{-1}.

(B) GCD curves at a current density of 1 mA cm^{-2}.

(C) CV curves of PAni/MnO_2@CC-300 s at different scan rates.

(D) GCD curves of PAni/MnO_2@CC-300 s at different current densities.

process, indicating a pseudocapacitive contribution. When b = 1, charge storage is mainly governed by a capacitive process, indicating an electric double-layer capacitance contribution.[35] As shown in Figure 7A, the values for the four peaks are 0.68, 0.86, 0.75, and 0.81, respectively, indicating that the energy storage mechanism of the sample is controlled by both capacitive and diffusion processes. To further quantify the proportion of these two charge storage mechanisms, the Dunn method is applied.[36] This can be calculated using Equation 2.

$$i(V) = k_1 v + k_2 v^{1/2} \quad \text{(Equation 2)}$$

where i is the total current (A) at a constant voltage (V), k_1 and k_2 are constants, which represents the current contribution controlled by capacitance, and $k_2 v^{1/2}$ represents the current contribution controlled by diffusion.[37,38] At a scan rate of 5 mV s^{-1}, the contributions of capacitance and diffusion mechanisms in the presence of the PAni/MnO_2@CC electrode are shown in Figure 7B. The closed curve represents the capacitance-controlled contribution, and the remaining area represents the contribution controlled by diffusion. As shown in Figure 7C, as the scan rate increases from 5 to 100 mV s^{-1}, the capacitance contribution increases from 11.8% to 38.4%. With the increase in scan rate, the capacitance-controlled contribution becomes more significant, indicating that the electrode material exhibits rapid kinetics and efficient ion diffusion characteristics. Correspondingly, the diffusion-controlled contribution gradually decreases. This behavior occurs because, at high scan rates, ions cannot fully penetrate the electrode layers or pores for intercalation/de-intercalation redox reactions, but can only participate in redox reactions with surface atoms or undergo physical adsorption/desorption on the electrode surface.

To further demonstrate the advantages of PAni/MnO_2@CC electrodes in practical applications, two identical PAni/MnO_2@CC electrodes were assembled into a symmetric supercapacitor (SC) using a PVA/H_2SO_4 gel electrolyte. Figure 8A shows the CV curves of the symmetric SC at various scan rates, ranging from 5 to 100 mV s^{-1}, within a potential range of 0–0.8 V. It can be observed that at high scan rates above 50 mV s^{-1}, the curves deviate from the rectangular shape and present a long spindle-like form, suggesting that the reaction in the SC tends to become irreversible. Furthermore, the peak currents are less defined, indicating diminished redox processes. However, the capacitive nature of the device is maintained even at high scan rates. The GCD curves at different current densities, as shown in Figure 8B, exhibit nearly symmetrical triangular shapes, indicating good electrochemical reversibility. The slight asymmetry of the triangular curves can be attributed to the pseudocapacitive behavior of both PAni and MnO_2, with their electrochemical behaviors mutually influencing one another. PAni and MnO_2 may exhibit different electrochemical activities within different potential ranges, and this potential mismatch may contribute to the asymmetry of the GCD curves. The variation of the areal capacitance of the symmetric SC with increasing scan rates is shown in Figure 8C. Based on Equations 4 and 5, the areal capacitance of the SC is calculated to be 287.8 mF cm^{-2} at a current density of 1 mA cm^{-2}, and 246.6 mF cm^{-2} at a current density of 5 mA cm^{-2}. Considering the loading mass of active materials, the gravimetric capacitance of the SC is calculated to be 285.4 F g^{-1} at a current density of 1 A g^{-1}, and 369.8 F g^{-1} at a current density of 2.5 A g^{-1}, demonstrating good rate performance. According to Equations 6, 7, 8, and 9, the assembled SC achieves an areal energy density of 25.58 μWh cm^{-2} at a power density of 477.9 μW cm^{-2} under 1 mA cm^{-2}, while the supercapacitor achieves an energy density of 25.37 Wh kg^{-1} at a power density of 804.6 W kg^{-1} at 1 A g^{-1}. Figure 8D shows the cycling stability of the PAni/MnO_2@CC symmetric SC after 2,000 charge-discharge cycles at a current density of 2.5 mA cm^{-2}, retaining 64.1% of its initial capacitance and 84.3% Coulombic efficiency. The notable drop on cycling retention could be attributed to two aspects: firstly,

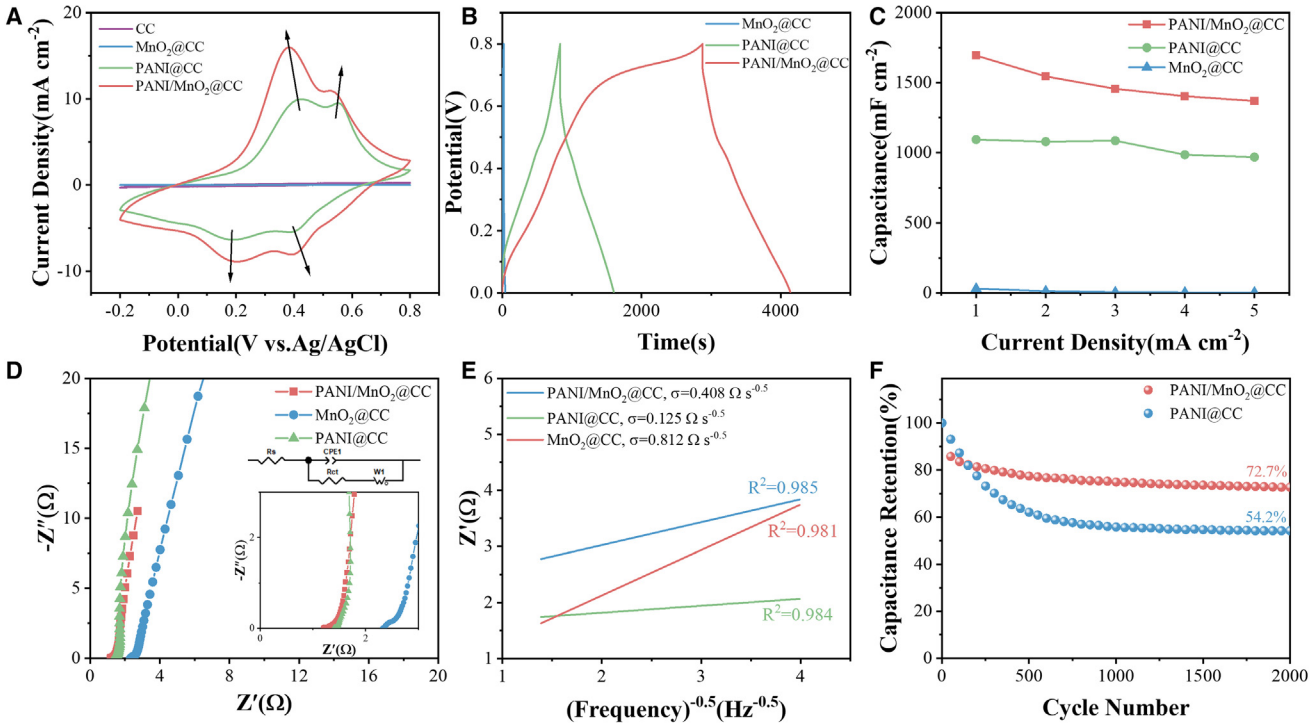

Figure 6. Plot of electrochemical properties of electrodes with different deposited materials

(A) CV curves of CC, MnO_2@CC, PAni@CC, and PAni/MnO_2@CC at a scan rate of 5 mV s^{-1}.

(B) GCD curves of MnO_2@CC, PAni@CC, and PAni/MnO_2@CC at a current density of 1 mA cm^{-2}.

(C) Specific capacitance at different current densities.

(D) EIS curves with the zoom view of the high frequency range as the inset.

(E) A linear fit of the real part of the impedance (z′) to the −1/2 power of the angular frequency curve ($\omega^{-0.5}$) in the low-frequency region (0.01–0.0825 Hz) was performed to extract the ion diffusion resistance.

(F) Cycling stability at 5 mA cm^{-2} for 2,000 cycles.

the long-time cycling could weaken the adhesion between PAni, MnO_2, and CC substrate, and interfacial delamination or mechanical stress results in detachment of the active materials; secondly, the high-resistance polymer electrolyte would accelerate the decomposition of electrolyte solutes and solvents in PAni/MnO_2@CC SC after long cycle times. For flexible energy storage devices, flexibility is also an important property. CV curves were obtained at different bending angles of 0°, 45°, and 90°, as shown in Figure 8E. Surprisingly, the flexible SC exhibits identical shapes across all bending angles from 0° to 90°,

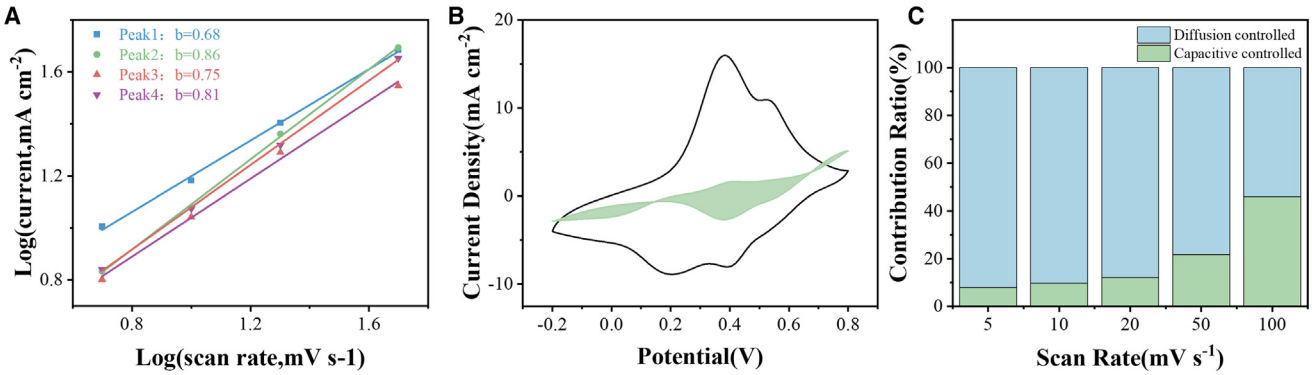

Figure 7. Kinetic analysis of PAni/MnO_2@CC

(A) Fitting lines of peak current versus scan rate.

(B) Capacitance and diffusion-controlled components at 5 mV s^{-1}.

(C) Normalized contributions of capacitance and diffusion-controlled components at different scan rates.

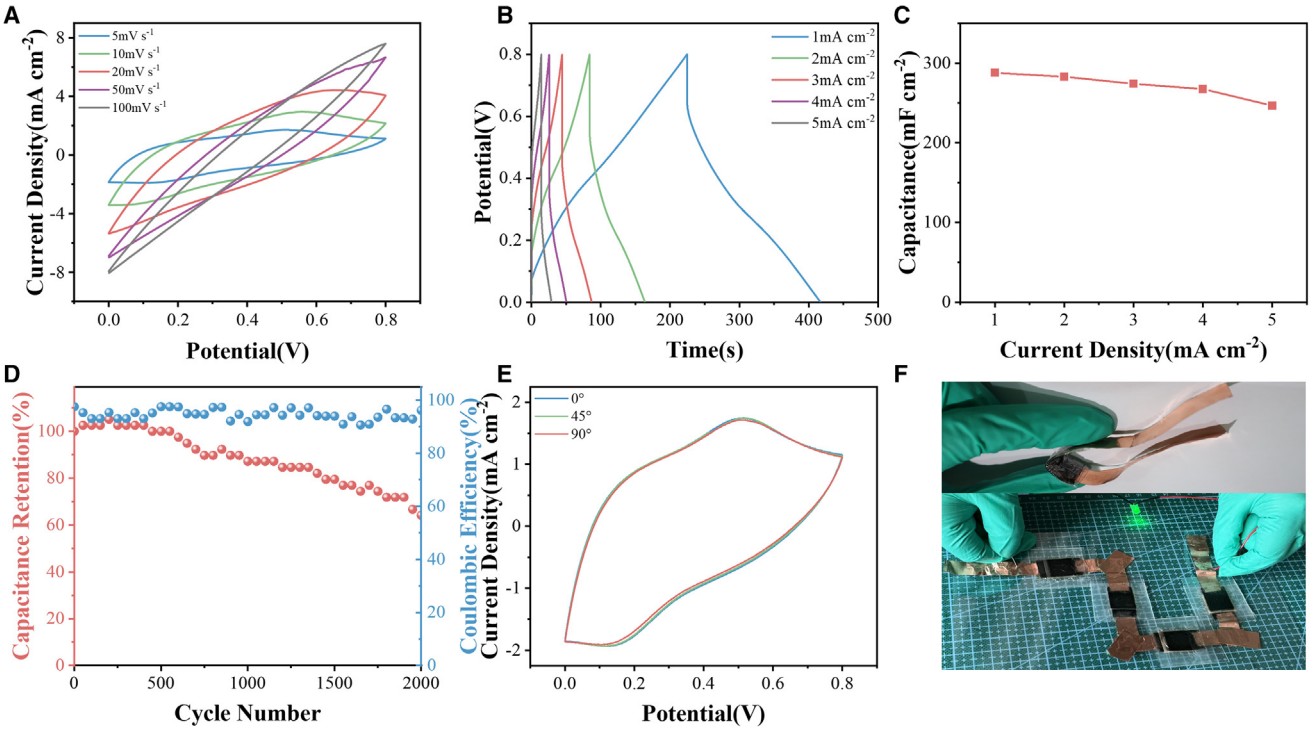

Figure 8. Electrochemical performance of the PAni/MnO_2@CC symmetric supercapacitor

(A) CV curves at different scan rates.

(B) GCD curves at different current densities.

(C) Specific capacitance at different current densities.

(D) Cycling stability at a current density of 2.5 mA cm^{-2}.

(E) Cyclic voltammetry curves at different bending angles.

(F) Optical image of the supercapacitor under bending (top) and the symmetric supercapacitors with 4 in series lighting an LED (3 V) (bottom).

illustrating its excellent flexibility. To further demonstrate the practical application potential of the obtained SC, four SCs connected in series were used to power a 3 V LED lamp for a period of time, as shown in the bottom image of Figure 8F.

To better demonstrate the capacitive characteristics of our assembled SC, the electrochemical properties have been compared with recently reported MnO_2-based or PAni-based SCs, as shown in Table 1. The one-step co-deposited PAni/MnO_2@CC SC in this work exhibits higher capacitance compared with the reported SCs with MnO_2/PAni electrode using hydrothermal method followed with *in situ* polymerization,[39] electrodeposition combined with chemical polymerization,[40] and dilute *in situ* polymerization method,[41] revealing that our fabrication method is advantageous offering both easy production and superior performance. Certainly, the obtained SC in this work delivers remarkably superior performance compared to other SCs with carbon material/PAni binary compositing cathodes.[42–44] As shown in the table, the SC device shows an energy density of 25.37 W h kg^{-1} at a power density of 804.6 W kg^{-1}. And this value is comparable with or higher than those of recently reported MnO_2-based or PAni-based supercapacitor devices. Results demonstrated that PAni/MnO_2@CC symmetric cell had the highest energy density mainly because of the high capacitance of the hybrid electrode. These findings suggest that PAni/MnO_2 composites, as active electrode materials, have good application potential in electrochemical supercapacitors.

DISCUSSION

In summary, the ternary PAni/MnO_2@CC composite electrode has been successfully fabricated through a simple and efficient one-step electrochemical deposition method. The synergistic effect of PAni and MnO_2 can significantly enhance the electrochemical performance of the PAni/MnO_2@CC electrode, which is approximately 1.6 times higher than that of the PAni@CC electrode and 50 times higher than that of the MnO_2@CC electrode. By investigating the effect of deposition time on electrochemical performance, the optimized electrode is obtained when the deposition time is 300 s, which exhibits the maximum specific capacitance (1,694.25 mF cm^{-2} at 1 mA cm^{-2}) and superior rate capability (capacitance retention of 80.8% from 1 to 5 mA cm^{-2}). Additionally, the assembled symmetric supercapacitor retains 64.1% of its initial specific capacitance after 2,000 cycles at a current density of 2.5 A cm^{-2}, and it provides an energy density of 25.58 μWh cm^{-2} at a power density of 477.9 μW cm^{-2}. This work offers a simple and effective approach for preparing high-performance symmetric supercapacitors.

Table 1. Comparison of the performance of the PAni/MnO2@CC supercapacitor device with previously reported PAni-based supercapacitors

Material	Electrolyte	Current density	Capacitance	Energy density	Power density	Ref.
MnO_2/PAni	0.5 M H_2SO_4	1 A g^{-1}	232.1 F g^{-1}	66.4 Wh kg^{-1}	350.1 W kg^{-1}	Zhu et al.[39]
PAni/MnO_2/PCNF	1 M H_2SO_4	1 A g^{-1}	289 F g^{-1}	119 Wh kg^{-1}	322 W kg^{-1}	Dirican, M et al.[40]
sGNS/MnO_2/PAni	1 M Na_2SO_4	1 A g^{-1}	276 F g^{-1}	–	–	Wang, G et al.[41]
mC/PAni	PVA/H_2SO_4	0.5 A g^{-1}	107.8 F g^{-1}	9.59 Wh kg^{-1}	980 W kg^{-1}	Noh, J et al.[42]
NCNT/PAni	PVA/H_2SO_4	2.47 A g^{-1}	128 F g^{-1}	11.1 Wh kg^{-1}	804.6 W kg^{-1}	Malik, R et al.[43]
ACTBs/PAni	1 M Na_2SO_4	1 A g^{-1}	154 F g^{-1}	42 Wh kg^{-1}	699 W kg^{-1}	Zhao, J et al.[44]
CC/MnO_2/PAni	PVA/H_2SO_4	1 A g^{-1}	285.4 F g^{-1}	25.37 Wh kg^{-1}	200.1 W kg^{-1}	our work
–	–	1 mA cm^{-2}	287.8 mF cm^{-2}	25.58 μWh cm^{-2}	477.91 μW cm^{-2}	–

Limitations of the study

As the conductive network in the electrode material, PAni can enhance the pseudocapacitive characteristics of the electrode, but it is prone to volume expansion and contraction during long-term cycling, which leads to structural instability and subsequently affects the capacitance retention. Therefore, although the proposed method shows potential to enhance electrochemical performance, further optimization is required to meet the demands of practical applications. This paper focuses on symmetric supercapacitors using PAni/MnO_2/CC as both electrodes, while future research will explore the performance of asymmetric supercapacitors.

RESOURCE AVAILABILITY

Lead contact

Further information and requests for resources and reagents should be directed to and will be fulfilled by the lead contact, Shuang Xi (shuangxi@njfu.edu.cn).

Materials availability

The study did not generate new unique materials. The readers can buy the chemicals to remake the materials as mentioned in the text.

Data and code availability

- All data reported in this paper will be shared by the lead contact upon request.
- This paper does not report the original code.
- Any additional information required to reanalyze the data reported in this paper is available from the lead contact upon request.

ACKNOWLEDGMENTS

This work received financial support from the National Natural Science Foundation of China (no. 52205457), the Guangdong Basic and Applied Basic Research Foundation, China (no. 2024A1515010043), and the Young Talent Support Project of Guangzhou Association for Science and Technology (no. QT2024-010).

AUTHOR CONTRIBUTIONS

Conceptualization, S.X., X.Q., and X.C.; writing – original draft, X.Q.; writing – review and editing, S.X. and H.L.; funding acquisition, H.L.; resources, S.X.; supervision, H.S. and D.D.

DECLARATION OF INTERESTS

The authors declare no competing interests.

STAR★METHODS

Detailed methods are provided in the online version of this paper and include the following:

- KEY RESOURCES TABLE
- EXPERIMENTAL MODEL AND SUBJECT DETAILS
- METHOD DETAILS
  - Materials
  - Synthesis of gel electrolyte
  - Fabrication of symmetric supercapacitor
  - Materials characterization
  - Electrochemical measurements
- QUANTIFICATION AND STATISTICAL ANALYSIS
- ADDITIONAL RESOURCES

Received: September 10, 2024
Revised: November 30, 2024
Accepted: January 7, 2025
Published: January 8, 2025

REFERENCES

1. Pershaanaa, M., Bashir, S., Ramesh, S., and Ramesh, K. (2022). Every bite of Supercap: A brief review on construction and enhancement of supercapacitor. J. Energy Storage *50*, 104599. https://doi.org/10.1016/j.est.2022.104599.
2. Liang, L., Li, L., Chen, R., Meng, J., Liu, H., Guo, C., Bao, W., Yao, D., Zhang, G., and Yu, F. (2024). Research advances in plant-derived activated carbon for electric double layer capacitors. J. Alloys Compd. *992*, 174641. https://doi.org/10.1016/j.jallcom.2024.174641.
3. Shen, H., Zhu, Y., Zada, I., Li, H., Bokhari, S.W., Zhu, S., and Li, Y. (2024). Investigation of strategies for improving the energy density of symmetric electrical double-layer capacitors. J. Energy Storage *79*, 110127. https://doi.org/10.1016/j.est.2023.110127.
4. Shi, Z., Wei, S., Zuo, H., Huang, M., Shi, J., and Wang, H. (2021). Boosting capacitance and energy density by construction NiCoO2/CoS2 nanocomposites arrays as pseudocapacitor. J. Alloys Compd. *881*, 160627. https://doi.org/10.1016/j.jallcom.2021.160627.
5. Wang, H., and Lee, J.-M. (2020). Recent advances in structural engineering of MXene electrocatalysts. J. Mater. Chem. A Mater. *8*, 10604–10624. https://doi.org/10.1039/D0TA03271A.
6. Malak-Polaczyk, A., Matei-Ghimbeu, C., Vix-Guterl, C., and Frackowiak, E. (2010). Carbon/λ-MnO2 composites for supercapacitor electrodes. J. Solid State Chem. *183*, 969–974. https://doi.org/10.1016/j.jssc.2010.02.015.
7. He, J., Zhou, Y., Wu, S., Jin, L., Cao, J., Demir, M., and Ma, P. (2024). Cr-Substituted SrCoO3-δ Perovskite with Abundant Oxygen Vacancies for High-Energy and Durable Low-Temperature Antifreezing Flexible

Supercapacitor. Inorg. Chem. *63*, 13755–13765. https://doi.org/10.1021/acs.inorgchem.4c02115.

8. Abdolahi, B., Gholivand, M.B., Shamsipur, M., and Amiri, M. (2022). Ordered mesoporous carbon/molybdenum carbide nanocomposite with high electrochemical performance asymmetric supercapacitor. J. Alloys Compd. *905*, 164185. https://doi.org/10.1016/j.jallcom.2022.164185.
9. Kale, A.M., Velayutham, R., Savariraj, A.D., Demir, M., and Kim, B.C. (2023). Unravelling the influence of interfacial tailoring in metal-organic framework-derived ultrathin sheets of Co2P/Cu3P for high-performance hybrid supercapacitor. Materials Today Sustainability *21*, 100335. https://doi.org/10.1016/j.mtsust.2023.100335.
10. Wu, Y., and Ran, F. (2017). Vanadium nitride quantum dot/nitrogen-doped microporous carbon nanofibers electrode for high-performance supercapacitors. J. Power Sources *344*, 1–10. https://doi.org/10.1016/j.jpowsour.2017.01.095.
11. Zhang, L., Chai, S.-S., Zhang, W.-B., Guo, S.-B., Han, X.-W., Guo, Y.-W., Bao, X., and Ma, X.-J. (2022). Cobalt boride on clay minerals for electrochemical capacitance. Appl. Clay Sci. *218*, 106416. https://doi.org/10.1016/j.clay.2022.106416.
12. Aydın, H., Kurtan, Ü., Üstün, B., Koç, S.N., Akgül, E., and Demir, M. (2024). A preparation of niobium diboride (NbB2) via molten salt method: Impact of boron concentration on the structural and electrochemical performance. Mater. Res. Bull. *180*, 113062. https://doi.org/10.1016/j.materresbull.2024.113062.
13. Khomenko, V., Frackowiak, E., and Béguin, F. (2005). Determination of the specific capacitance of conducting polymer/nanotubes composite electrodes using different cell configurations. Electrochim. Acta *50*, 2499–2506. https://doi.org/10.1016/j.electacta.2004.10.078.
14. Lota, K., Khomenko, V., and Frackowiak, E. (2004). Capacitance properties of poly(3,4-ethylenedioxythiophene)/carbon nanotubes composites. J. Phys. Chem. Solid. *65*, 295–301. https://doi.org/10.1016/j.jpcs.2003.10.051.
15. Rajesh, M., Raj, C.J., Kim, B.C., Cho, B.-B., Ko, J.M., and Yu, K.H. (2016). Supercapacitive studies on electropolymerized natural organic phosphate doped polypyrrole thin films. Electrochim. Acta *220*, 373–383. https://doi.org/10.1016/j.electacta.2016.10.118.
16. Liu, R., Jiang, R., Chu, Y., and Yang, W.D. (2021). Facile Fabrication of MnO2/Graphene/Ni Foam Composites for High-Performance Supercapacitors. Nanomaterials *11*, 2736.
17. Wang, S., Huo, W., Fang, F., Xie, Z., Shang, J.K., and Jiang, J. (2022). High entropy alloy/C nanoparticles derived from polymetallic MOF as promising electrocatalysts for alkaline oxygen evolution reaction. Chem. Eng. J. *429*, 132410. https://doi.org/10.1016/j.cej.2021.132410.
18. Song, N., Wu, Y., Wang, W., Xiao, D., Tan, H., and Zhao, Y. (2019). Layer-by-layer in situ growth flexible polyaniline/graphene paper wrapped by MnO2 nanoflowers for all-solid-state supercapacitor. Mater. Res. Bull. *111*, 267–276. https://doi.org/10.1016/j.materresbull.2018.11.024.
19. Tan, H., Xiao, D., Navik, R., and Zhao, Y. (2021). Facile Fabrication of Polyaniline/Pristine Graphene–Bacterial Cellulose Composites as High-Performance Electrodes for Constructing Flexible All-Solid-State Supercapacitors. ACS Omega *6*, 11427–11435. https://doi.org/10.1021/acsomega.1c00442.
20. Sun, X., Gan, M., Ma, L., Wang, H., Zhou, T., Wang, S., Dai, W., and Wang, H. (2015). Fabrication of PANI-coated honeycomb-like MnO2 nanospheres with enhanced electrochemical performance for energy storage. Electrochim. Acta *180*, 977–982. https://doi.org/10.1016/j.electacta.2015.09.056.
21. Zhu, Y., Xu, H., Chen, P., Bao, Y., Jiang, X., and Chen, Y. (2022). Electrochemical performance of polyaniline-coated γ-MnO2 on carbon cloth as flexible electrode for supercapacitor. Electrochim. Acta *413*, 140146. https://doi.org/10.1016/j.electacta.2022.140146.
22. Huo, W., Wang, S., Fang, F., Tan, S., Kurpaska, Ł., Xie, Z., Kim, H.S., and Jiang, J. (2022). Microstructure and corrosion resistance of highly <111> oriented electrodeposited CoNiFe medium-entropy alloy films. J. Mater. Res. Technol. *20*, 1677–1684. https://doi.org/10.1016/j.jmrt.2022.07.175.
23. Yang, R., Guo, Z., Cai, L., Zhu, R., Fan, Y., Zhang, Y., Han, P., Zhang, W., Zhu, X., Zhao, Q., et al. (2021). Investigation into the Phase–Activity Relationship of MnO2 Nanomaterials toward Ozone-Assisted Catalytic Oxidation of Toluene. Small *17*, 2103052. https://doi.org/10.1002/smll.202103052.
24. Tong, Z., Yang, Y., Wang, J., Zhao, J., Su, B.-L., and Li, Y.J. (2014). Layered polyaniline/graphene film from sandwich-structured polyaniline/graphene/polyaniline nanosheets for high-performance pseudosupercapacitors. J. Mater. Chem. A *2*, 4642–4651.
25. Chen, L., Sun, L.-J., Luan, F., Liang, Y., Li, Y., and Liu, X.X. (2010). Synthesis and pseudocapacitive studies of composite films of polyaniline and manganese oxide nanoparticles. J. Power Sources *195*, 3742–3747.
26. Cao, X., Liu, Y., Zhong, Y., Cui, L., Zhang, A., Razal, J.M., Yang, W., and Liu, J. (2020). Flexible coaxial fiber-shaped asymmetric supercapacitors based on manganese, nickel co-substituted cobalt carbonate hydroxides. J. Mater. Chem. A Mater. *8*, 1837–1848. https://doi.org/10.1039/C9TA11942F.
27. Huang, M., Li, F., Dong, F., Zhang, Y.X., and Zhang, L.L. (2015). MnO2-based nanostructures for high-performance supercapacitors. J. Mater. Chem. A Mater. *3*, 21380–21423. https://doi.org/10.1039/C5TA05523G.
28. Abdolahi, B.S., Gholivand, M.B., Shamsipur, M., and Amiri, M. (2023). Introduction of a three-dimensional flower-like Mo2CTx/poly (2, 2′-dithiodianiline) on reduced graphene oxide as an efficient electrode for supercapacitor and hydrogen evolution reaction. J. Energy Storage *62*, 106906.
29. Ansari, S.A., Parveen, N., Han, T.H., Ansari, M.O., and Cho, M.H. (2016). Fibrous polyaniline@manganese oxide nanocomposites as supercapacitor electrode materials and cathode catalysts for improved power production in microbial fuel cells. Phys. Chem. Chem. Phys. *18*, 9053–9060. https://doi.org/10.1039/C6CP00159A.
30. Mezgebe, M.M., Xu, K., Wei, G., Guang, S., and Xu, H. (2019). Polyaniline wrapped manganese dioxide nanorods: Facile synthesis and as an electrode material for supercapacitors with remarkable electrochemical properties. J. Alloys Compd. *794*, 634–644. https://doi.org/10.1016/j.jallcom.2019.04.295.
31. El-Khodary, S.A., El-Enany, G.M., El-Okr, M., and Ibrahim, M. (2017). Modified iron doped polyaniline/sulfonated carbon nanotubes for all symmetric solid-state supercapacitor. Synth. Met. *233*, 41–51. https://doi.org/10.1016/j.synthmet.2017.09.002.
32. Krishnamoorthy, K., Pazhamalai, P., Sahoo, S., and Kim, S.-J. (2017). Titanium carbide sheet based high performance wire type solid state supercapacitors. J. Mater. Chem. A Mater. *5*, 5726–5736. https://doi.org/10.1039/C6TA11198J.
33. Liu, H., Zheng, Y., Moon, K.-S., Chen, Y., Shi, D., Chen, X., and Wong, C.-P. (2022). Ambient-air in situ fabrication of high-surface-area, superhydrophilic, and microporous few-layer activated graphene films by ultrafast ultraviolet laser for enhanced energy storage. Nano Energy *94*, 106902. https://doi.org/10.1016/j.nanoen.2021.106902.
34. Wang, Q., Niu, B., Han, Y., Zheng, Q., Li, L., and Cao, M. (2023). Nature-inspired 3D hierarchical structured "vine" for efficient microwave attenuation and electromagnetic energy conversion device. Chem. Eng. J. *452*, 139042. https://doi.org/10.1016/j.cej.2022.139042.
35. Chen, L., Chen, L., Zhai, W., Li, D., Lin, Y., Guo, S., Feng, J., Zhang, L., Song, L., Si, P., and Ci, L. (2019). Tunable synthesis of LixMnO2 nanowires for aqueous Li-ion hybrid supercapacitor with high rate capability and ultra-long cycle life. J. Power Sources *413*, 302–309. https://doi.org/10.1016/j.jpowsour.2018.12.026.
36. Cheng, H., Chen, X., Yu, H., Guo, M., Chang, Y., and Zhang, G.J. (2020). Hierarchically porous N, P-codoped carbon materials for high-performance supercapacitors. ACS Appl. Energy Mater. *3*, 10080–10088.
37. Amiri, A., Naraghi, M., and Polycarpou, A.A. (2022). Zinc-ion hybrid supercapacitors with ultrahigh areal and gravimetric energy densities and long

cycling life. J. Energy Chem. *70*, 480–491. https://doi.org/10.1016/j.jechem.2022.03.029.

38. Yang, F., Guo, H., Zhang, J., Wu, N., Yang, M., Chen, Y., Zhang, T., Sun, L., and Yang, W.J. (2022). Core–shell structured WS2@ Ni-Co-S composite and activated carbon derived from rose flowers as high-efficiency hybrid supercapacitor electrodes. J. Energy Storage *54*, 105234.
39. Zhu, Y., Xu, H., Tang, J., Jiang, X., Bao, Y., and Chen, Y. (2021). Synthesis of γ-MnO2/PANI Composites for Supercapacitor Application in Acidic Electrolyte. J. Electrochem. Soc. *168*, 030542. https://doi.org/10.1149/1945-7111/abef82.
40. Dirican, M., Yanilmaz, M., Asiri, A.M., and Zhang, X. (2020). Polyaniline/MnO2/porous carbon nanofiber electrodes for supercapacitors. J. Electroanal. Chem. *861*, 113995. https://doi.org/10.1016/j.jelechem.2020.113995.
41. Wang, G., Tang, Q., Bao, H., Li, X., and Wang, G. (2013). Synthesis of hierarchical sulfonated graphene/MnO2/polyaniline ternary composite and its improved electrochemical performance. J. Power Sources *241*, 231–238. https://doi.org/10.1016/j.jpowsour.2013.04.122.
42. Noh, J., Jekal, S., and Yoon, C.-M. (2023). Polyaniline-Coated Mesoporous Carbon Nanosheets with Fast Capacitive Energy Storage in Symmetric Supercapacitors. Adv. Sci. *10*, 2301923. https://doi.org/10.1002/advs.202301923.
43. Malik, R., Zhang, L., McConnell, C., Schott, M., Hsieh, Y.-Y., Noga, R., Alvarez, N.T., and Shanov, V. (2017). Three-dimensional, free-standing polyaniline/carbon nanotube composite-based electrode for high-performance supercapacitors. Carbon *116*, 579–590. https://doi.org/10.1016/j.carbon.2017.02.036.
44. Zhao, J., Li, Y., Chen, X., Zhang, H., Song, C., Liu, Z., Zhu, K., Cheng, K., Ye, K., Yan, J., et al. (2018). Polyaniline-modified porous carbon tube bundles composite for high-performance asymmetric supercapacitors. Electrochim. Acta *292*, 458–467. https://doi.org/10.1016/j.electacta.2018.09.178.

STAR★METHODS

KEY RESOURCES TABLE

REAGENT or RESOURCE	SOURCE	IDENTIFIER
Chemicals, peptides, and recombinant proteins		
Carbon cloth	Taiwan Carbon Energy Technology Co., Ltd	W0S1011
Cellulose diaphragm	Tianjin Aiweixin Chemical Technology Co., Ltd	H-100
Manganese sulfate monohydrate	Sinopharm Chemical Reagent Co., Ltd	CAS:10034-96-5
Polyvinyl alcohol	Sinopharm Chemical Reagent Co., Ltd	CAS:9002-89-5
Sulfuric acid	Guangzhou Hewei Pharmaceutical Technology Co., Ltd	CAS:7647-01-0
Aniline	Sinopharm Chemical Reagent Co., Ltd	CAS: 62-53-3
Software and algorithms		
OriginLab	Analyze and graph	https://www.originlab.com
Other		
Electrochemical workstation CHI-660E	Charging and discharging	http://www.chinstr.com

EXPERIMENTAL MODEL AND SUBJECT DETAILS

There are no experimental models (animals, human subjects, plants, microbe strains, cell lines, primary cell cultures) used in the study.

METHOD DETAILS

Materials

The raw materials utilized in this study are listed as following: Carbon cloth (W0S1011), manganese sulfate monohydrate (AR), Cellulose diaphragm (H-100), polyvinyl alcohol (GR), sulfuric acid (H_2SO_4), aniline (AR). Preparation of PAni/MnO_2@CC electrode.

First, the carbon cloth (CC) was cut into 1.5 * 2 cm^2 pieces and clean with deionized water followed with ethanol. The one-step electrochemical deposition process was conducted in depositing solution of 1 M H_2SO_4, 0.1 M aniline and 0.1 M $MnSO_4 \cdot H_2O$, with CC served as the working electrode, Ag/AgCl as the reference electrode, and a platinum plate as the counter electrode. PAni and MnO_2 were simultaneously deposited on the CC surface using chronoamperometry at 1.4 V. The prepared samples were washed with ethanol and deionized water for multiple times, and then dried in a vacuum oven at 60°C for 24 h to obtain PAni/MnO_2@CC electrode. To investigate the effect of depositing thickness on the electrochemical performance of hybrid electrode, different deposition durations were selected with 100 s, 300 s and 500 s, where the sample was denoted as PAni/MnO_2@CC-100s, PAni/MnO_2@CC-300s and PAni/MnO_2@CC-500s, respectively. The thickness of the electrode is approximately 0.42 mm. In order to comparatively analyze the synergistic effect of PAni and MnO_2 for electrodes, PAni@CC and MnO_2@CC was also fabricated using the abovementioned procedure only removing the addition of $MnSO_4 \cdot H_2O$ or aniline monomer in depositing solution, respectively.

Synthesis of gel electrolyte

The preparation of PVA/H_2SO_4 gel electrolyte is as follows: 2 g of PVA was added to 20 mL of 1 M H_2SO_4 solution and magnetically stirred for 20 min at room temperature to ensure PVA completely dissolved. Then, the solution was continuously stirred at 85°C until it became viscous and clear. Finally, the solution was poured into the mold and the transparent PVA/H_2SO_4 gel electrolyte was obtained after cooling naturally to room temperature.

Fabrication of symmetric supercapacitor

The PVA/H_2SO_4 gel electrolyte with the thickness of 1.5 mm was applied to two identical PAni/MnO_2@CC electrodes. A Cellulose diaphragm (H-100) was placed between the two electrodes to prevent short circuits. The two electrodes were assembled face-to-face to form a sandwich-structured symmetric supercapacitor. For testing, two copper foils were connected to the two PAni/MnO_2@CC electrodes. Finally, the assembled supercapacitor was left to sit at room temperature for 2-3 h to remove any excess moisture.

Materials characterization

The morphology of the samples was investigated using a scanning electron microscope (SEM, JSM-7600F), a transmission electron microscope (TEM, JEM-1400) and high-resolution transmission electron microscopy (HR-TEM, JEM-2100 UHR). The structural properties of the prepared samples were studied using X-ray diffraction (XRD) with an XRD Ultima IV. The chemical structure and elemental composition of the composite electrode surfaces were characterized using X-ray photoelectron spectroscopy (XPS) with an AXIS UltraDLD.

Electrochemical measurements

The electrochemical performance of the prepared electrodes was tested using electrochemical workstation (CHI 660E, Chenhua Instruments, China) under three-electrode in 1M H_2SO_4 electrolyte solution, with the prepared sample as the working electrode, platinum plate serving as the counter electrode and Ag/AgCl as reference electrode. Cyclic voltammetry (CV), galvanostatic charge-discharge (GCD), and electrochemical impedance spectroscopy (EIS) tests were carried out.

Based on the GCD curves, the areal capacitance C_1 (mF cm^{-2}) of PAni/MnO_2@CC in the three-electrode system and symmetric supercapacitor devices can be calculated using Equation 3.

$$C_1 = \frac{I\Delta t}{S\Delta V} \quad \text{(Equation 3)}$$

Where ΔV (V) is the voltage window excluding the voltage drop during discharge, Δt (s) is the discharge time, S (cm^2) is the actual working area of the electrode, and I (A) is the discharge current.

The areal capacitance C_2 (mF cm^{-2}), the specific capacitance C_3 (F g^{-1}), areal energy density E_A (μWh cm^{-2}), areal power density P_A (μW cm^{-2}), specific energy density E_s (Wh kg^{-1}) and specific power density P_s (W kg^{-1}) of the symmetric supercapacitor were calculated in the two-electrode system by the following Equations 4, 5, 6, 7, 8, and 9.

$$C_2 = \frac{I\Delta t}{S\Delta V} \quad \text{(Equation 4)}$$

$$C_3 = \frac{I\Delta t}{m\Delta V} \quad \text{(Equation 5)}$$

$$E_A = \frac{1}{2}C_2 \times \frac{(\Delta V)^2}{3.6} \quad \text{(Equation 6)}$$

$$P_A = \frac{E_A}{\Delta t} \times 3600 \quad \text{(Equation 7)}$$

$$E_s = \frac{1}{2}C_3 \times \frac{(\Delta V)^2}{3.6} \quad \text{(Equation 8)}$$

$$P_s = \frac{E_A}{\Delta t} \times 3600 \quad \text{(Equation 9)}$$

Where ΔV (V) is the actual discharge voltage window, m is the weight of the active materials and Δt (s) is the discharge time.

QUANTIFICATION AND STATISTICAL ANALYSIS

No methods were used to determine whether the data met the assumptions of the statistical approach.

ADDITIONAL RESOURCES

Our study has not generated or contributed to a new website/forum or has not been part of a clinical trial.